Synchronous Estimation Scheme of PMSM Mechanical Parameters: A Decoupled Extended Sliding-Mode Observer

He Chang, *Student Member, IEEE*, Zuo Wang, *Member, IEEE*, Jun Yang, *Fellow, IEEE*, Shihua Li, *Fellow, IEEE*, and Shaowu Lu

***Abstract*—In the permanent magnet synchronous motor drives (PMSM), high-quality controller optimization and condition monitoring rely heavily on accurate knowledge of mechanical parameters. To address this need, this study presents a novel decoupled extended sliding-mode observer (DESMO) capable of achieving high-quality synchronous estimation of the moment of inertia and the load disturbance. An extended state-space equation is, first, constructed by extending the mechanical equations. Subsequently, the novel DESMO is designed by introducing two new recursive equations. On this basis, the excitation weight on the moment of inertia is analyzed, resulting in the derivation of Lyapunov-mechanism-based decoupling updating conditions (DOCs) to further exploit the DESMO's estimation potential. Furthermore, when the DOCs are not all satisfied, the second observation equation is derived with the reaching law of the moment of inertia set to zero to achieve state decoupling during estimation process. With the switching excitation of DOCs, notably, the DESMO is capable of serving as a more competitive candidate for observing multimechanical parameters, as demonstrated through simulation and experimental results.**

***Index Terms*—Decoupled extended sliding-mode observer (DESMO), decoupling updating conditions (DOCs), load disturbance, moment of inertia, parameter identification, permanent magnet synchronous motor (PMSM).**

Received 25 August 2024; revised 20 December 2024 and 19 February 2025; accepted 7 April 2025. Date of publication 14 April 2025; date of current version 26 May 2025. The work was supported in part by the National Natural Science Foundation of China under Grant 62103102, Grant 62173221, Grant 62025302, and Grant 52475525, in part by the Jiangsu Funding Program for Excellent Postdoctoral Talent under Grant 2024ZB055, in part by the China Postdoctoral Science Foundation under Grant 2024M750423, and in part by the SEU Innovation Capability Enhancement Plan for Doctoral Students under Grant CXJH_SEU 24130. Recommended for publication by Associate Editor Ali M. Bazzi. *(Corresponding authors: Zuo Wang; Jun Yang.)*

He Chang, Zuo Wang, and Shihua Li are with the School of Automatin, Southeast University, Nanjing 210096, China, and also with the Key Laboratory of Measurement and Control of CSE, Ministry of Education, Nanjing 210096, China (e-mail: h.chang@seu.edu.cn; z.wang@seu.edu.cn; lsh@seu.edu.cn).

Jun Yang is with the Department of Aeronautical and Automotive Engineering, Loughborough University, LE11 3TU Loughborough, U.K. (e-mail: j.yang3@lboro.ac.uk).

Shaowu Lu is with the School of Information Science and Engineering, Wuhan University of Science and Technology, Wuhan 430081, China (e-mail: shawn2013@wust.edu.cn).

Color versions of one or more figures in this article are available at https://doi.org/10.1109/TPEL.2025.3560352.

Digital Object Identifier 10.1109/TPEL.2025.3560352

I. Introduction

DUE to its high torque-to-inertia ratio and superior power density, the permanent magnet synchronous motor (PMSM) dominates a wide range of application markets that require fast response and high efficiency, such as electric vehicles, computer numerical control (CNC) machine tools, and manipulators [1], [2], [3]. However, these characteristics also present unique challenges for control optimization and condition monitoring. For example, the high torque-to-inertia ratio requires the control system to be capable of adapting to rapid inertia variations [3], while the increased power density also amplifies the impact of load torque and nonlinear disturbances on system stability [4]. Thus, both the high torque-to-inertia ratio and superior power density place higher demands on the high-performance controller and the condition monitoring system. It should be noted that in the PMSM-based servo system, high-quality controller optimization, and condition monitoring are generally inseparable from knowledge of inertia and load disturbance. Not surprisingly, real-time inertia monitoring can adjust controller parameters to improve control performance [3], and feedforward compensation based on the load disturbance is able to enhance the system's disturbance rejection ability [5]. However, estimating accurate moment of inertia and load disturbance information in many scenarios is quite challenging due to variable conditions and complex environments. Therefore, it is of practical significance to develop an identification technique for synchronous estimation of both moment of inertia and load disturbance.

In recent years, considerable attention has been devoted by scholars to the simultaneous estimation of mechanical parameters. Initially, the extended Kalman filter is popular due to insensitivity to Gaussian white noise, but its computational complexity were unfriendly to engineers [6], [7]. To reduce the computational burden, some algorithms on the combination of recursive algorithm and disturbance observer were proposed [8], [9]. However, these recursive algorithms (the recursive frequency-domain algorithm in [8] and the improved recursive least-squares algorithm in [9]) also involve matrix operation, and their robustness is relatively poor. Interestingly, some disturbance-observer-based composite estimation methods (DOCEMs) were studied and capable of overcoming the shortcoming of complexity [10], [11], [12]. For example, an extended

sliding-mode observer (ESMO) was proposed in [10] to observe the lumped disturbance, and after two identical acceleration processes, the estimation of inertia can be simply obtained. Similarly, after observing the disturbance by the ESMO, two methods, direct computation and proportional integration, were designed to accomplish the asymptotic estimation of inertia, and concluded that these methods were more suitable for offline identification [11]. To further enhance the estimation performance, a finite-time disturbance observer was proposed and combined with a model-referenced adaptive system to estimate the inertia [12]. Nevertheless, these DOCEMs do not guarantee the observation accuracy and overall convergence of load disturbance for an initial given of unknown inertia, in particular under large modeling errors [13]. Fortunately, benefiting from the integral property to offset load disturbances during periodic inertia estimation, periodic command quadrature techniques are remarkable for their asymptotic convergence and robustness. However, the strict speed command and the inertia updating problem at zero-speed and zero-crossing points impose challenges for further development [14], [15], [16], [17].

Parallel estimation techniques, in which two observers are utilized to estimate mechanical parameters in a parallel interactive manner, have attracted increasing attention [3], [18], [19], [20], [21]. In [18] and [19], an ESMO and an Adaline estimator were developed simultaneously for estimating the inertia and load disturbance. Still, the global convergence of multiobserver is not guaranteed, implying that it may bring about difficulties in choosing own parameters and uncertainties in the identification results. In [20], [21], [22], more notably, parallel ESMOs (PESMOs) were proposed by designing the interconnected gains between the states, and could solve the above problems and further improve robustness. However, these methods are limited by the following deficiencies.

1) The parallel-interaction property between states tends to cause dynamic coupling in the estimation process, thereby sacrificing the estimation performance.
2) It has to be assumed that the derivatives of inertia and load disturbances are zero, which potentially harms the reliability of error convergence, in particular under complex operating conditions.
3) The global convergence guarantee for multiple states is not proven; it is only demonstrated that the sliding-mode surface of the overall network is reachable.

Recently, it is worth noting that the two-state idea-based observer has emerged as an effective tool to simultaneously estimate the moment of inertia and lumped disturbance [23], [24], [25]. In [23], a two-state ESMO (TESMO) was proposed by designing a robust activator to remove the transient-state coupling relationship between two states. This idea was also implemented in the extended disturbance observer in [24] by designing a trigger with an inverse tangent function. In [25], a variable structure ESMO (VSESMO) was designed to achieve decoupling between the estimation states and the derivative of sliding-mode surface, thereby eliminating the chattering phenomenon. Although some efforts have been made above toward the first prerequisite, the transient-state and steady-state coupling relationships between the states and the interaction of their excitation weights need to be further analyzed to motivate the estimation potential. In conclusion, it is still worth exploring an identification technique to achieve high-quality estimation of the total inertia and load disturbance.

Based on the abovementioned analysis, a two-state-based decoupled ESMO (DESMO) is proposed in this article. The main contributions are summarized as follows.

1) Based on an extended state-space equation, the novel DESMO is developed by introducing two recursive equations. Then, by analyzing the excitation weight of the moment of inertia, Lyapunov-mechanism-based decoupling updating conditions (DOCs) are designed to improve the estimation performance.
2) In the case that not all DOCs hold, a new observation equation in which the reaching law on the moment of inertia is set to zero is derived to achieve state decoupling in the estimation process. This not only avoids strong dynamic coupling between states, but also ensures a fast estimation of load disturbance.
3) In contrast to these observers in [20], [21], [22], [23], [24], and [25], based on the switching incentives of the DOCs, our DESMO is able to further release the potential for realizing high-quality online estimation and remove the assumption that the derivatives of the parameters are assumed to be zero. In addition, the stability proofs of the two update equations in our DESMO are rigorously derived.

II. Analysis of the Existing SMO-Based Estimation Methods

A. Modeling of the PMSM Servo System

In the context of the dq-axis reference frame, and employing field-oriented vector control with d-axis current $i_d^* = 0$, the dynamic equations on the PMSM servo system are conventionally articulated as follows [26]:

$$\begin{cases} \dot{\omega}_m = m_j(T_e - T_f), \dot{m}_j = d_1, \dot{T}_f = d_2 \\ T_e = K_t i_q, m_j = \frac{1}{J_m} \\ T_f = B_m\omega_m + C_m \text{sgn}(\omega_m) + T_L + D \end{cases} \tag{1}$$

where ω_m, J_m, T_e, K_t, i_q, and T_f are the motor speed, the moment of inertia, the electromagnetic torque, the torque coefficient, the torque current, and the load disturbance, respectively. B_m, C_m, T_L, and D denote, respectively, the viscous friction coefficient, the Coulomb friction coefficient, the load torque, and the unknown disturbance (unmodeled dynamics, and other harmonic disturbances). sgn() denotes the sign function. m_j denotes the reciprocal of J_m. d_1 and d_2 are the derivatives of m_j and T_f with respect to time t, respectively.

B. Analysis of the PESMO

The PESMO is to design two ESMOs with time-varying reaching laws to estimate the moment of inertia and the load disturbance simultaneously based on the state interconnection

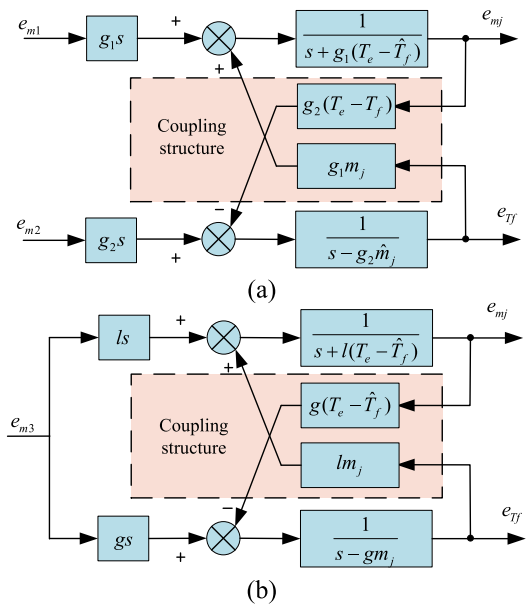

Fig. 1. (a) S-domain block diagram of the PESMO in [22]. (b) S-domain block diagram of the TESMO in [23].

property, and it is specifically expressed as follows [22]:

$$O_1: \begin{cases} \dot{\hat{\omega}}_{m1} = (T_e - \hat{T}_f)\cdot \hat{m}_j + k_1 \mathrm{sgn}(S_1) \\ \dot{\hat{m}}_j = q_1(T_e - \hat{T}_f) k_1 \mathrm{sgn}(S_1) \end{cases} \tag{2}$$

$$O_2: \begin{cases} \dot{\hat{\omega}}_{m2} = (T_e - \hat{T}_f)\cdot \hat{m}_j + k_2 \mathrm{sgn}(S_2) \\ \dot{\hat{T}}_f = -q_2 \hat{m}_j k_2 \mathrm{sgn}(S_2) \end{cases} \tag{3}$$

where $q_1 > 0$ and $q_2 > 0$. k_1 and k_2 are the sliding-mode switching gains. $\hat{\omega}_{m1}$ and $\hat{\omega}_{m2}$ stand for the estimated values of ω_m. $\hat{T}_f$ and $\hat{m}_j$ are the estimated values of T_f and m_j, respectively. The sliding-mode surfaces are $S_1 = \hat{\omega}_{m1} - \omega_m$ and $S_2 = \hat{\omega}_{m2} - \omega_m$. Note that the authors define $g_1 = q_1(T_e - \hat{T}_f)$ and $g_2 = -q_2 \hat{m}_j$ as the interconnected gains.

Suppose that $d_1 = d_2 = 0$, subtracting (1) from (2) and (3), respectively, yields the corresponding error equations, which are then processed as

$$g_1 \dot{e}_{m1} = \dot{e}_{mj} + g_1(T_e - \hat{T}_f) e_{mj} - g_1 m_j e_{Tf} \tag{4}$$

$$g_2 \dot{e}_{m2} = \dot{e}_{Tf} + g_2(T_e - T_f) e_{mj} - g_2 \hat{m}_j e_{Tf} \tag{5}$$

where $e_{m1} = \hat{\omega}_{m1} - \omega_m$, $e_{m2} = \hat{\omega}_{m2} - \omega_m$, $e_{mj} = \hat{m}_j - m_j$, and $e_{Tf} = \hat{T}_f - T_f$.

From (4) and (5), it is concluded that the errors e_{mj} and e_{Tf} have the ability of converging gradually to zero as the sliding-mold surfaces are reached, i.e., $\dot{e}_{m1} = \dot{e}_{m2} = 0$. After performing the Laplace transform to (4) and (5), however, as illustrated in the error equation block schematic in Fig. 1(a), the two states in the PESMO are severally coupled to each other, which will deteriorate the estimation performance of the results.

C. Analysis of the TESMO

The TESMO is to design two adaptive laws to estimate the moment of inertia and load disturbance under the forcing of one sliding mode, and it is represented as follows [23]:

$$\begin{cases} \dot{\hat{\omega}}_{m3} = (T_e - \hat{T}_f)\cdot \hat{m}_j + u \\ \dot{\hat{m}}_j = lu, \dot{\hat{T}}_f = gu \end{cases} \tag{6}$$

where $l = l_0 \mathrm{sgn}(T_e - \hat{T}_f)$, $l_0 > 0$, $g > 0$. $\hat{\omega}_{m3}$ is the estimated value of ω_m. $u = -k_3 S_3 - \varepsilon \mathrm{sgn}(S_3)$, and $S_3 = \hat{\omega}_{m3} - \omega_m$ denotes the sling-mode surface. k_3 and ε denote the sliding-mode switching gain and the robust gain, respectively. Consequently, (6) is able to be processed as

$$\dot{S}_3 = \dot{\hat{\omega}}_{m3} - \dot{\omega}_{m3} = u + (T_e - \hat{T}_f)\cdot e_{mj} - m_j e_{Tf}. \tag{7}$$

Assuming that $d_1 = d_2 = 0$, based on (6) and (7), the error equations on $\hat{T}_f$ and $\hat{m}_j$, can be described as

$$\dot{e}_{mj} = \dot{\hat{m}}_j - d_1 = l\dot{e}_{m3} - l(T_e - \hat{T}_f) e_{mj} + l m_j e_{Tf} \tag{8}$$

$$\dot{e}_{Tf} = \dot{\hat{T}}_f - d_2 = g\dot{e}_{m3} - g(T_e - \hat{T}_f) e_{mj} + g m_j e_{Tf}. \tag{9}$$

It can be seen from (8) and (9) that, similar to the PESMO, the errors e_{mj} and e_{Tf} converge exponentially to zero when the sliding-mode surface is reached. Meanwhile, performing the Laplace transform to (8) and (9), as shown in Fig. 1(b), they also suffer from the same defect, i.e., the presence of a coupling between the two state terms. Thus, a state decoupling method proposed in [23] is to redesign $l_0 = l_g \max\{|v_d - v_m| - \Delta_\omega, 0\}$, where l_g and Δ_ω stand for the gain coefficient and the threshold value, respectively.

Remark 1: It is noted from Fig. 1 that the two ESMOs mentioned above have a highly similar structure, with specific differences in the number of input errors and the design of adaptive laws. Specifically, this results in the two observers exhibiting varying degrees of state coupling during the estimation process. Furthermore, it can be found from Fig. 1 that in addition to the existence of the coupling structure, the system transfer functions $\frac{1}{s+g_1(T_e-\hat{T}_f)}$ and $\frac{1}{s-g_2\hat{m}_j}$ in the PESMO and the system transfer function $\frac{1}{s+l(T_e-\hat{T}_f)}$ in the TESMO exhibit respective coupling.

Remark 2: In recent years, scholars have conducted foundational research in this area [23], [24]. For example, the robust activator in [23] and the trigger in [24] aim to redesign the reaching law of moment of inertia to mitigate the coupling effects. Nevertheless, it is clear that they have not provided a comprehensive and effective solution for the state coupling effects, nor have they conducted rigorous stability proofs. Furthermore, both ESMOs that require the derivatives of the estimation parameters to be zero is clearly unfavorable for the estimation of T_f and m_j with time-varying properties. Therefore, in the following section, a novel DESMO will be proposed to tackle the aforementioned challenges, with the capability to deliver high-quality parameter estimation performance.

III. Design of the DESMO

Hence, in the proposed DESMO, by extending (1), a new extended-state equation is constructed as follows:

$$\begin{bmatrix} \dot{z}_1(t) \\ \dot{z}_2(t) \\ \dot{z}_3(t) \end{bmatrix} = \begin{bmatrix} 0 & 1 & 0 \\ 0 & 0 & \dot{T}_e(t) \\ 0 & 0 & 0 \end{bmatrix} \begin{bmatrix} z_1(t) \\ z_2(t) \\ z_3(t) \end{bmatrix} + \begin{bmatrix} D_0(t) \\ D_1(t) \\ D_2(t) \end{bmatrix} \tag{10}$$

$$\begin{cases} D_0(t) = m_{j0}T_e(t) - T_{d0}, T_{d0} = m_{j0}T_{f0} \\ D_1(t) = \dot{\bar{m}}_j(t)T_e(t) - \dot{\bar{T}}_d \\ D_2(t) = \dot{\bar{m}}_j(t), \bar{m}_j(t) = m_j(t) - m_{j0} \\ \bar{T}_d(t) = T_d(t) - T_{d0}, T_d(t) = m_j(t)T_f(t) \end{cases} \tag{11}$$

where m_{j0} and T_{f0} denote the initial to-be-given values. $z_1(t) = \omega_m(t)$, $z_2(t) = \bar{m}_j(t)T_e(t) - \bar{T}_d(t)$, and $z_3(t) = m_j(t) - m_{j0}$. Note that $\dot{\bar{m}}_j(t) = \dot{m}_j(t)$ and $\dot{\bar{T}}_d(t) = \dot{T}_d(t)$. To observe (10), the DESMO is designed as

$$\begin{aligned} \begin{bmatrix} \dot{\hat{z}}_1(t) \\ \dot{\hat{z}}_2(t) \\ \dot{\hat{z}}_3(t) \end{bmatrix} &= \begin{bmatrix} 0 & 1 & 0 \\ 0 & 0 & \dot{T}_e(t) \\ 0 & 0 & 0 \end{bmatrix} \begin{bmatrix} \hat{z}_1(t) \\ \hat{z}_2(t) \\ \hat{z}_3(t) \end{bmatrix} + \begin{bmatrix} D_0(t) \\ 0 \\ 0 \end{bmatrix} \\ &+ \begin{bmatrix} F_1(k_4, k_5) \\ F_2(f_1, f_3, k_4, k_5) \\ F_3(f_2, f_4, k_4, k_5, \dot{T}_e(t)) \end{bmatrix} \text{sgn}(S) \end{aligned} \tag{12}$$

where $\hat{z}_1$, $\hat{z}_2$, and $\hat{z}_3$ stand for the estimated values of z_1, z_2, and z_3. f_1, f_2, f_3, and f_4 denote the reaching laws that only require $f_1 > 0$, $f_2 > 0$, $f_3 > 0$, and $f_4 = 0$. k_4 and k_5 are the sliding-mode switching gains. $S = \omega_m(t) - \hat{\omega}_m(t)$ denotes the sliding-mode surface, where $\hat{\omega}_m$ is the estimated value of ω_m. F_1, F_2, and F_3 denote the to-be-designed decoupling functions. It is important to note that several remarks need to be elicited in order to more clearly illuminate the advantages of the proposed observer and the subsequent stability analysis.

Remark 3: In this DESMO, both $m_j(t)$ and $T_d(t)$ can be calculated by a simple decoupling shown in (13). Letting $\tilde{m}_j(t) = m_j(t) - \hat{m}_j(t)$ and $\tilde{T}_d(t) = T_d(t) - \hat{T}_d(t)$, the error equations on $m_j(t)$ and $T_d(t)$ are given by (14), where $\tilde{z}_2(t) = z_2(t) - \hat{z}_2(t)$, $\tilde{z}_3(t) = z_3(t) - \hat{z}_3(t)$. $\hat{m}_j(t)$ and $\hat{T}_d(t)$ denote, respectively, the estimated values of $m_j(t)$ and $T_d(t)$. As a consequence, on can get that the errors $\tilde{m}_j(t)$ and $\tilde{T}_d(t)$ are capable of converging to zero, if the terms $\hat{z}_2$ and $\hat{z}_3$ are able to track z_2 and z_3 precisely

$$\begin{cases} m_j(t) = z_3(t) + m_{j0} \\ T_d(t) = z_3(t)T_e(t) + T_{d0} - z_2(t) \end{cases} \tag{13}$$

$$\begin{cases} \tilde{m}_j(t) = \tilde{z}_3(t) \\ \tilde{T}_d(t) = \tilde{z}_3(t)T_e(t) - \tilde{z}_2(t). \end{cases} \tag{14}$$

Remark 4: It is worth noting from (10) to (12) that the excitation weight of $z_3(t)$ come from $\dot{T}_e(t)$, i.e., the greater the amplitude of $\dot{T}_e(t)$, the greater the effect of $z_3(t)$ on the DESMO system. Conversely, if the value of $\dot{T}_e(t)$ is very small, the estimate of $z_3(t)$ is susceptible to noise. Accordingly, since the excitation weight of $z_2(t)$ is a constant, taking the weighting factor of $z_3(t)$ as a reference standard to design the DOCs can further exploit the potential of the observer. In addition, the reaching law on the inertia is set to zero, $f_4 = 0$, to achieve the state decoupling in the estimation process in the case that when the DOCs do not all hold. Consequently, the decoupling functions can be processed as

$$F_1(k_4, k_5) = \begin{cases} k_4, \text{The DOCs hold} \\ k_5, \text{Else} \end{cases}$$

$$F_2(f_1, f_3, k_4, k_5) = \begin{cases} f_1 k_4, \text{The DOCs hold} \\ f_3 k_5, \text{Else} \end{cases}$$

$$F_3(f_2, k_4, k_5, \dot{T}_e(t)) = \begin{cases} f_2 k_4 \dot{T}_e(t), \text{The DOCs hold} \\ f_4 k_5 \dot{T}_e(t), \text{Else.} \end{cases} \tag{15}$$

Based on the design analysis of the DESMO, if all the DOCs hold, subtracting (11) from (12) yields the following error equations, where $\tilde{z}_1(t) = z_1(t) - \hat{z}_1(t)$

$$\dot{\tilde{z}}_1(t) = \tilde{z}_2(t) - k_4 \text{sgn}(S) \tag{16}$$

$$\dot{\tilde{z}}_2(t) = \dot{T}_e(t)\tilde{z}_3(t) + D_1(t) - f_1 k_4 \text{sgn}(S) \tag{17}$$

$$\dot{\tilde{z}}_3(t) = D_2(t) - f_2 \dot{T}_e(t) k_4 \text{sgn}(S). \tag{18}$$

Conversely, if the DOCs do not all hold, the error equations are given by

$$\dot{\tilde{z}}_1(t) = \tilde{z}_2(t) - k_5 \text{sgn}(S) \tag{19}$$

$$\dot{\tilde{z}}_2(t) = \dot{T}_e(t)\tilde{z}_3(t) + D_1(t) - f_3 k_5 \text{sgn}(S) \tag{20}$$

$$\dot{\tilde{z}}_3(t) = D_2(t) - f_4 k_5 \dot{T}_e(t) \text{sign}(S). \tag{21}$$

Assumption 1: It is generally recognized that there exists $|\dot{\omega}_m^*(t)| \le N_0$ in the reference speed command $\omega_m^*(t)$, where N_0 is positive constant. For the design of the subsequent part of the DOCs, consequently, some reasonable assumptions based on the physical characteristics of the PMSM servo system are defined as $N_1 \le m_j(t) \le N_2$, $|\dot{m}_j(t)| \le N_3$, $|T_d(t)| \le N_4$, $N_5 \le |\dot{T}_d(t)| \le N_6$, where N_1, N_2, N_3, N_4, N_5, and N_6 are all positive constants. Due to the amplitude limitation of the speed controller output, there exists $N_7 > 0$ such that $|T_e(t)| \le N_7$. As a result, we can obtain that $D_0(t) \le m_{j0}N_7 - T_{d0}$, $D_1(t) \le N_3 N_7 - N_5$, and $D_2(t) \le N_3$.

IV. Stability Analysis of the DESMO

Here, since the DOCs result in the existence of two update equations for the DEMSO, two stability analyzes need to be derived to validate the feasibility of our scheme. Before that, as in other sliding-mode observers, the convergence of the sliding-mode surface should be verified.

A. Convergence Analysis of the Sliding-Mode Surface

According to (11) and (12), the derivative of the sliding-mode surface S with respect to time t is given by

$$\begin{aligned} \dot{S}(t) &= \dot{\omega}_m(t) - \dot{\hat{\omega}}_m(t) \\ &= \tilde{m}_j(t)T_e(t) - \tilde{T}_d(t) - F_1(k_4, k_5)\text{sgn}(S). \end{aligned} \tag{22}$$

Then, a Lyapunov candidate is chosen as $V(t) = \frac{1}{2}S^2$, and it is derivative with respect to time t is deduced by

$$\begin{aligned} \dot{V}(t) &= [\tilde{m}_j(t)T_e(t) - \tilde{T}_d(t) - F_1(k_4, k_5)\text{sgn}(S)] \cdot S \\ &= d \cdot S - F_1(k_4, k_5) \cdot |S| \\ &\le -(F_1(k_4, k_5) - \bar{d}) \cdot |S| \\ &= -\sqrt{2}(F_1(k_4, k_5) - \bar{d})V^{0.5} \end{aligned} \tag{23}$$

where $\bar{d} = \sup|\tilde{m}_j(t)T_e(t) - \tilde{T}_d(t)|$ and $d = \tilde{m}_j(t)T_e(t) - \tilde{T}_d(t)$. Solving (23) yields that when (24) is satisfied, $V(t)$

will converge to zero in finite time $T_0 = -\frac{\sqrt{2}}{F_1(k_4,k_5)-d}V^{0.5}(0)$. Therefore, the sliding-mode surface will reach to zero in T_0

$$F_1(k_4,k_5) > \sup\left|\tilde{m}_j(t)T_e(t) - \tilde{T}_d(t)\right|. \tag{24}$$

Hence, for the two updating equations, it need to be ensured that $k_4 > \sup|\tilde{m}_j(t)T_e(t) - \tilde{T}_d(t)|$ and $k_5 > \sup|\tilde{m}_j(t)T_e(t) - \tilde{T}_d(t)|$.

Assumption 2: From (23) and (24), it is observed that the convergence of the sliding-mode surface S brings $\tilde{z}_1(t) = 0$, so one reasonable assumption can be obtained that $|\dot{\tilde{z}}_1(t)| \le N_7$, where $N_7 > 0$.

B. Stability Analysis With Satisfying all the DOCs

Here, (17) minus (16) multiplied by f_1 gives (25), and (18) minus (16) multiplied by $f_2\dot{T}_e(t)$ yields (26)

$$\dot{\tilde{z}}_2(t) = -f_1\tilde{z}_2(t) + \dot{T}_e(t)\tilde{z}_3(t) + \bar{D}_1(t) \tag{25}$$

$$\dot{\tilde{z}}_3(t) = -f_2\dot{T}_e(t)\tilde{z}_2(t) + \bar{D}_2(t) \tag{26}$$

where $\bar{D}_1(t) = \dot{\tilde{m}}_j(t)T_e(t) - \dot{\tilde{T}}_d + f_1\dot{\tilde{z}}_1(t)$ and $\bar{D}_2(t) = \dot{\tilde{m}}_j(t) + f_2\dot{\tilde{z}}_1(t)$.

Select a Lyapunov candidate as $V_{z1}(t) = \varepsilon^{\mathrm{T}}(t)P_{z1}(t)\varepsilon(t)$, where $\varepsilon(t) = [\tilde{z}_2(t) \quad \tilde{z}_3(t)]^{\mathrm{T}}$ and $P_{z1}(t)$ is a symmetric positive definite matrix yielded by the Lyapunov equation and is given by

$$P_{z1}(t) = \begin{bmatrix} \frac{f_2+1}{2f_1} & -\frac{1}{2}\dot{T}_e^{-1}(t) \\ -\frac{1}{2}\dot{T}_e^{-1}(t) & \frac{f_2+1}{2f_1f_2} + \frac{f_1}{2f_2}\dot{T}_e^{-2}(t) \end{bmatrix}. \tag{27}$$

Next, the derivation of $\varepsilon(t)$ to time t is obtained as follows:

$$\dot{\varepsilon}(t) = \begin{bmatrix} \dot{\tilde{z}}_2(t) \\ \dot{\tilde{z}}_3(t) \end{bmatrix} = A_{z1}(t)\varepsilon(t) + B_{z1}(t) \tag{28}$$

$$A_{z1}(t) = \begin{bmatrix} -f_1 & \dot{T}_e(t) \\ -f_2\dot{T}_e(t) & 0 \end{bmatrix} \tag{29}$$

$$B_{z1}(t) = \begin{bmatrix} \bar{D}_1(t) & \bar{D}_2(t) \end{bmatrix}^{\mathrm{T}} \tag{30}$$

where $A_{z1}(t)$ satisfies the definition of a Hurwitz matrix, if the DOC I, which need to be set to $\alpha_1 \le |\dot{T}_e(t)| \le \alpha_2$, holds, where α_1 and α_2 are to-be-adjusted positive parameters. Thus, based on (27) and (30), under Assumptions 1 and 2, it is evident to derive (31), where $N_8 > 0$

$$\|P_{z1}(t)B_{z1}(t)\| \le N_8 \text{ for } t \ge 0. \tag{31}$$

Theorem 1: There exits a positive constant $0 < \kappa < 1$ such that the symmetric positive definite matrix $\phi(t) \in \mathbb{R}^{2\times 2} = \kappa I_2 - \dot{P}_{z1}(t)$ is valid, if all DOCs I–III hold, where the DOCs II and III is, respectively, designed as follows:

$$\begin{cases} \text{The DOC II}: \ |\dot{T}_e(t)| \le \alpha_3 \text{ for } t \ge 0 \\ \text{The DOC III}: \ \left|\ddot{T}_e(t)\right| \le \alpha_4 \text{ for } t \ge 0. \end{cases} \tag{32}$$

Proof: It should be noted that due to $A_{z1}(t)$ is a Hurwitz matrix and the DOC I holds, the matrix $P_{z1}(t)$ with time-varying properties is subject to the maximum eigenvalue $\lambda_{\max}\{P_{z1}\}$ and minimum eigenvalue $\lambda_{\min}\{P_{z1}\}$. At the same time, if the DOCs II and III holds, the derivative of symmetric definite matrix $P_{z1}(t)$ with respect to time t is processed as

$$\dot{P}_{z1}(t) = \begin{bmatrix} 0 & \frac{1}{2}\dot{T}_e^{-2}(t)\ddot{T}_e(t) \\ \frac{1}{2}\dot{T}_e^{-2}(t)\ddot{T}_e(t) & -\frac{f_1}{f_2}\dot{T}_e^{-3}(t)\ddot{T}_e(t) \end{bmatrix}. \tag{33}$$

Hence, to ensure the positive definiteness of $\phi(t)$, it needs to satisfy the following conditions:

$$\kappa > 0 \tag{34}$$

$$\begin{vmatrix} \kappa & -\frac{1}{2}\dot{T}_e^{-2}(t)\ddot{T}_e(t) \\ -\frac{1}{2}\dot{T}_e^{-2}(t)\ddot{T}_e(t) & \kappa + \frac{f_1}{f_2}\dot{T}_e^{-3}(t)\ddot{T}_e(t) \end{vmatrix} > 0. \tag{35}$$

We observe from (34) and (35) that the positive definiteness of $\phi(t)$ is readily ensured by a simple adjustment of α_4. So, the proof is complete. It can be concluded that, therefore, there exits a symmetric positive definite matrix such that

$$\varepsilon^T(t)\phi(t)\varepsilon(t) \ge 0 \text{ for } t \ge 0. \tag{36}$$

Theorem 2: For any initial values m_{j0} and T_{f0}, the errors $\tilde{z}_2(t)$ and $\tilde{z}_3(t)$ will be eventually consistently bounded, if there are to-be-adjusted positive parameters such that all of the DOCs I–III hold.

Proof: See Appendix A

C. Stability Analysis Without Satisfying all the DOCs

Here, rewriting (19)–(21) yields

$$\dot{\tilde{z}}_1(t) = \tilde{z}_2(t) - k_5\text{sgn}(S) \tag{37}$$

$$\dot{\tilde{z}}_2(t) = D_3(t) + D_1(t) - f_3k_5\text{sgn}(S) \tag{38}$$

where $D_3(t) = \dot{T}_e(t)\tilde{z}_3(t)$, so it is not difficult to conclude that there exists a positive constant $N_9 > 0$ such that $D_3(t) \le N_9$, and in addition, $D_3(t)$ is negligible as $\tilde{z}_3$ tends to zero. Then, according to Assumptions 1 and 2, subtracting (37) multiplied by f_3 from (38) yields

$$\begin{aligned} \dot{\tilde{z}}_2(t) &= -f_3\tilde{z}_2(t) + D_3(t) + D_1(t) + f_3\dot{\tilde{z}}_1(t) \\ &\le -f_3\tilde{z}_2(t) + N_9 + N_3N_6 - N_5 + f_3N_7. \end{aligned} \tag{39}$$

Hence, regarded as the first-order time-varying differential equation, the error equation (39) is solved as

$$\tilde{z}_2(t) \le [\int(N_9 + N_3N_6 - N_5 + f_3N_7)e^{\int f_3 \mathrm{d}t}\mathrm{d}t + N_{10}]e^{-\int f_3 \mathrm{d}t} \tag{40}$$

where N_{10} represents the initial observation error values. Thus, the condition for $\tilde{z}_2$ to converge exponentially is $f_3 > 0$.

Remark 5: We observe from (47) and (40) that the proposed DESMO maintains its stability in both updating equations and removes the assumption that the derivatives of the parameters are assumed to be zero during the design process. The schematic and s-domain analysis of the error equation are shown in Fig. 2 . It can be seen that the design of the DOCs enables the proposed DESMO to minimize coupling effects between states. Moreover,

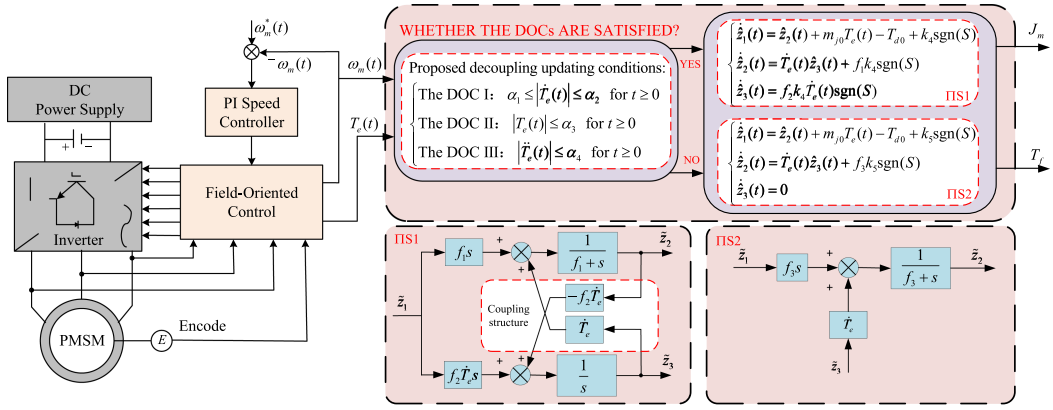

Fig. 2. Schematic diagram of the proposed DESMO.

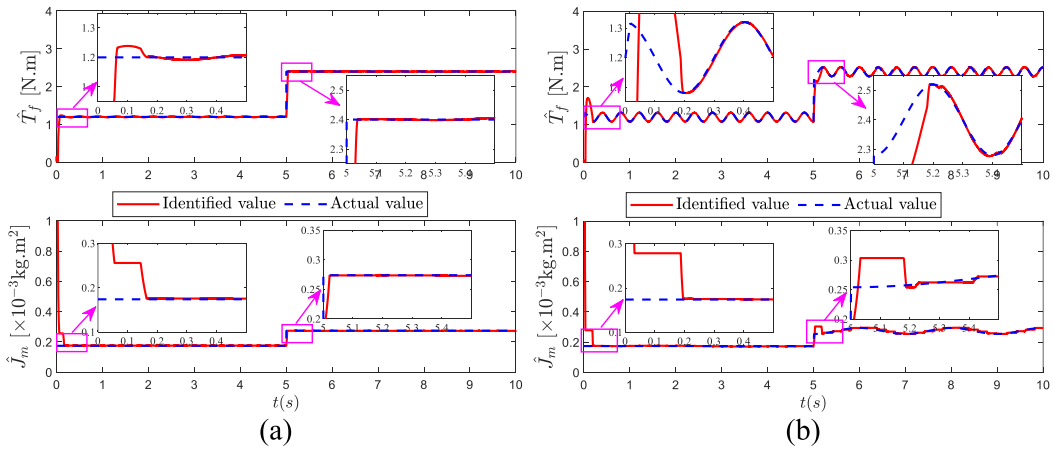

Fig. 3. Simulation results of the proposed DESMO. (a) Under the case that $B_m = 0$. (b) Under the case that $B_m \neq 0$.

due to its unique properties, the system transfer functions $\frac{1}{f_1+s}$ and $\frac{1}{s}$ do not involve estimated states, further avoiding state coupling between them.

Remark 6: It should be emphasized that the parameter configuration of the DOCs is critical but easier to regulate. Specifically, α_1, α_2, and α_3 are the main parameters to be regulated, where α_3 needs to be regulated first because it is not sensitive to the observer. Then, for the parameters α_1 and α_2, the difference in amplitude between the two ends of $|\dot{T}_e(t)|$ is generally no more than 5. The parameter α_4 is negligible to improve the estimation performance, and therefore, can in general be simply ignored. It is noted that the abovementioned theoretical derivation makes multiple use of the electromagnetic torque signal. While some undesirable noise may cause slight shifts in the electromagnetic torque, the DOCs of the proposed observer remain robustly insensitive to such perturbations. In addition, to avoid the chattering phenomena of the sliding-mode observer, sgn() can be replaced by the following saturation function, where $\Delta_S > 0$ denotes the boundary layer [23]

$$\text{sat}(S) = \begin{cases} S/\Delta_S, & \text{if } |\text{S}| < \Delta_\text{S} \\ \text{sgn}(S), & \text{if } |\text{S}| \ge \Delta_\text{S} \end{cases} \tag{41}$$

TABLE I
RELATIVE PARAMETERS OF THE PMSM

Parameter	Unit	Value
Torque coefficient	$\text{N} \cdot \text{m/A}$	0.14
Pole pairs	\	5
Moment of inertia	$\text{kg} \cdot \text{m}^2$	1.74×10^{-4}
Rated speed	r/min	3000
Viscous friction coefficient	$\text{N} \cdot \text{m} \cdot \text{s} \cdot \text{rad}^{-1}$	4×10^{-4}
Rated torque	$\text{N} \cdot \text{m}$	2.4

V. SIMULATION AND EXPERIMENTAL RESULTS

A. Simulation Result

In this section, it is necessary for the proposed method to implement simulation through MATLAB/Simulink to verify effectiveness. The system parameters of the PMSM driver are shown in Table I, and the parameter configurations for the proposed DESMO and the four comparative observers proposed in [22], [23], and [25] are presented in Table II.

In order to comprehensively evaluate the advantages of the proposed method, we will classify the simulation conditions into two cases: $B_m = 0$ and $B_m \neq 0$. Figs. 3 and 4 exhibit

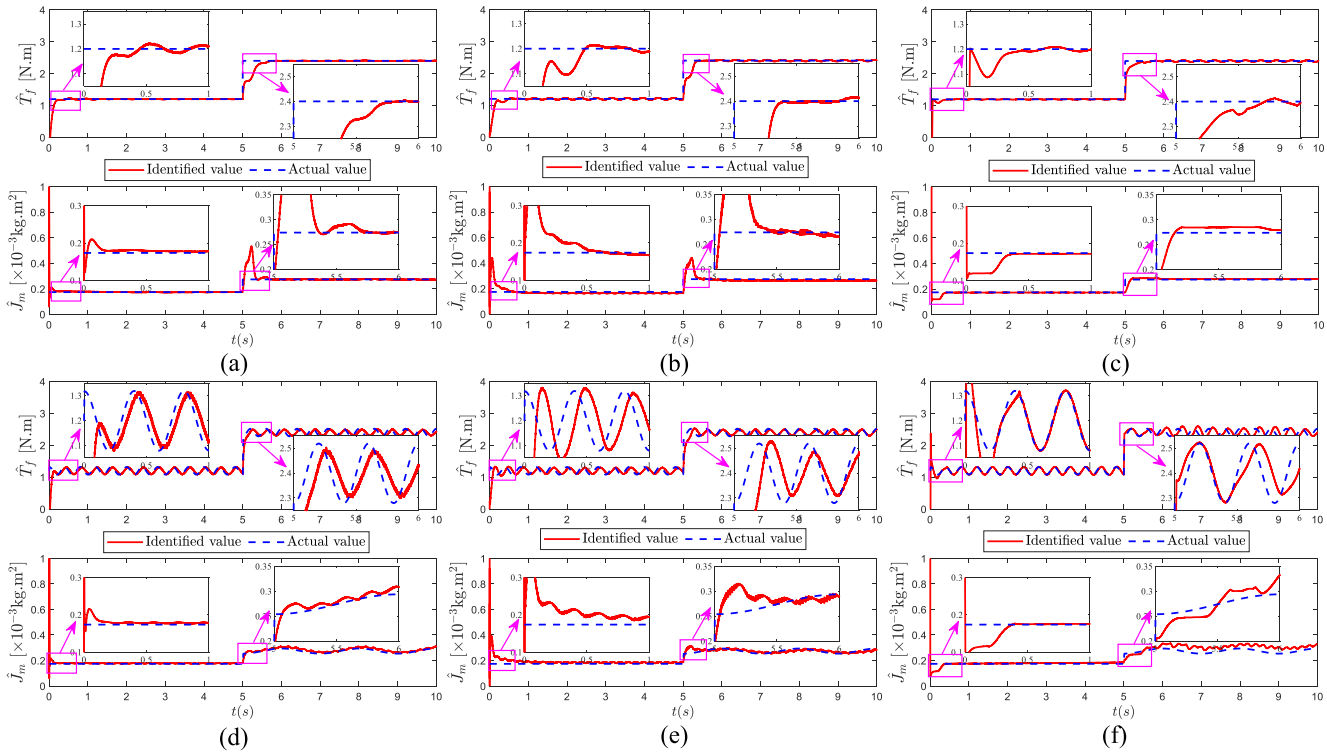

Fig. 4. Simulation results of the compared methods. (a) and (d) are from the PESMO in [22]. (b) and (e) are from the VSESMO in [25], (c) and (f) are from the TESMO in [23]; (a)–(c) Under the case that $B_m = 0$; (b)–(f) Under the case that $B_m \neq 0$.

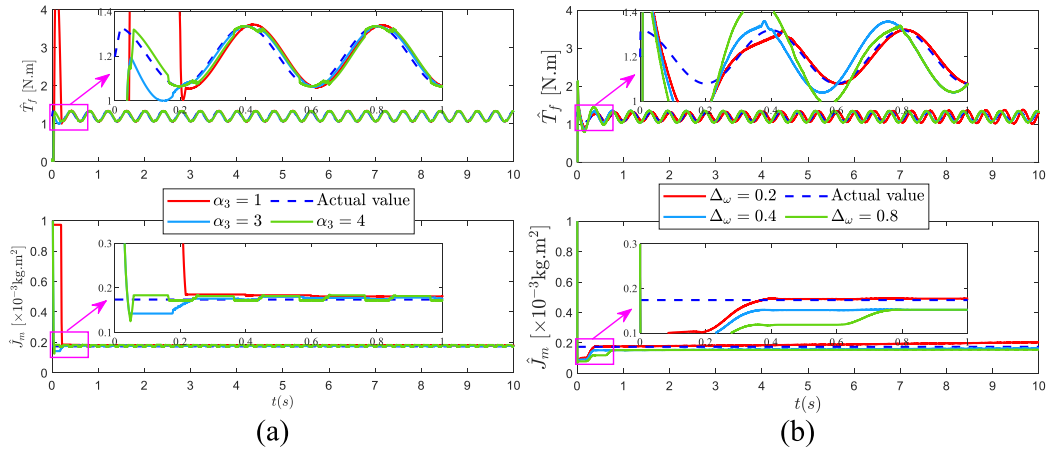

Fig. 5. (a) Simulation results of our DESMO with different α_3. (b) Simulation results of the TESMO in [23] with different Δ_ω.

TABLE II
PARAMETER CONFIGURATION WITH DIFFERENT METHODS

Methods	Our DESMO	The PESMO in [22]	The VSESMO in [25]	The TESMO in [23]
Parameter settings in simulation	$k_1 = 1500$, $k_2 = 2000$, $f_1 = 160$, $f_2 = 0.003$, $f_3 = 100$, $\alpha_1 = 2$, $\alpha_2 = 150$, $\alpha_3 = 2$, $\alpha_4 = 2000$.	$k_1 = -12000$, $q_1 = 9$, $k_2 = -20000$, $q_2 = 1 \times 10^{-6}$.	$\gamma = -50000$, $\lambda = 150$, $\beta = -2000$.	$k = 8000$, $\varepsilon = 1000$, $l_g = 10$, $g = 0.0012$, $\Delta_\omega = 0.6$.
Parameter settings in experiment	$k_1 = 5000$, $k_2 = 7000$, $f_1 = 80$, $f_2 = 0.0008$, $f_3 = 80$, $\alpha_1 = 4$, $\alpha_2 = 150$, $\alpha_3 = 2$, $\alpha_4 = 4000$.	$k_1 = -15000$, $q_1 = 9$, $k_2 = -20000$, $q_2 = 9 \times 10^{-7}$.	$\gamma = -60000$, $\lambda = 180$, $\beta = -3000$.	$k = 12000$, $\varepsilon = 1000$, $l_g = 4$, $g = 0.0012$, $\Delta_\omega = 0.4$.
Initial value settings	$\hat{z}_1(0) = 0$, $\hat{z}_2(0) = 0$, $\hat{z}_3(0) = 100$	$\hat{m}_j(0) = 100$, $\hat{T}_f(0) = 0$.		
Speed command	$\omega_m^*(t) = 300 \times \cos(2\pi \cdot 2.5 \cdot t)$.			

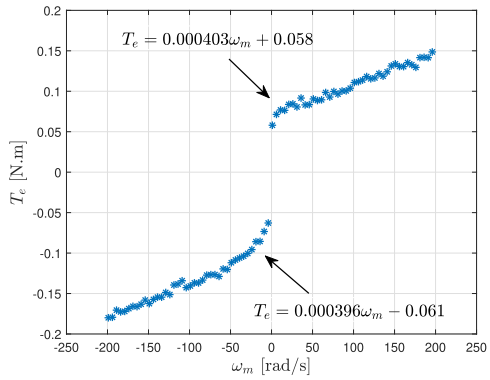

Fig. 6. Fitting curve of friction coefficients.

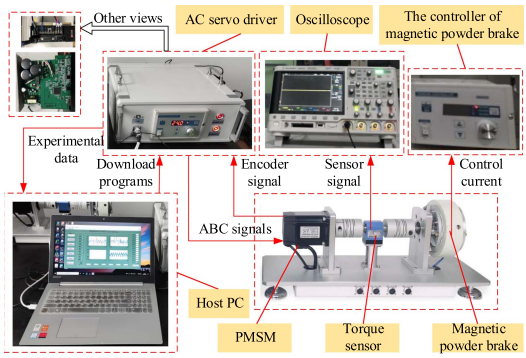

Fig. 7. Experimental testing platform.

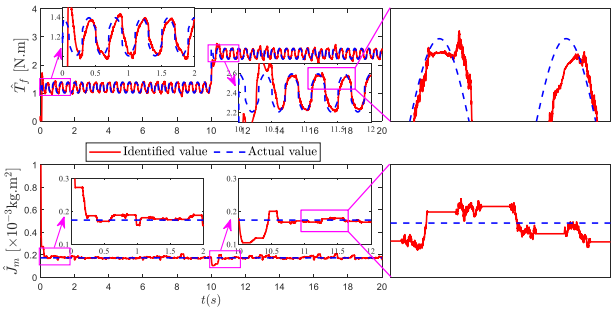

Fig. 8. Experimental results of the proposed DESMO.

the simulation results of the four observers under these two cases. It can be observed that the TESMO, equipped with the robust activator, converges to the actual value in approximately 0.4 s. In contrast, due to the dynamic coupling effects between states, the PESMO and VSESMO require at least 0.5 s to achieve stable convergence in both cases. Benefiting from the decoupling properties of the proposed DOCs, our DESMO demonstrates superior performance, converging to the actual value in just about 0.2 s across both scenarios.

It is worth noting that in the case of $B_m \neq 0$, the time-varying load disturbance imposes significant challenges on the PESMO, VSESMO, and TESMO observers due to the assumption that

TABLE III
QUANTITATIVE COMPARISON OF THE THREE OBSERVERS

Contents	$\hat{J}_m$		$\hat{T}_f$	
	CT(s)	RMSE	CT(s)	RMSE
Fig. 3(a) on DESMO	0.185s	0.328e 5	0.188s	0.0457
Fig. 3(b) on DESMO	0.192s	0.649e 5	0.196s	0.0643
Fig. 4(a) on PESMO	0.875s	2.785e 5	1.081s	0.1145
Fig. 4(b) on VSESMO	0.604s	2.120e 5	0.682s	0.0992
Fig. 4(c) on TESMO	0.368s	0.927e 5	0.436s	0.0566
Fig. 4(d) on PESMO	0.539s	0.898e 5	0.223s	0.0779
Fig. 4(e) on VSESMO	0.754s	1.509e 5	0.463s	0.0937
Fig. 4(f) on TESMO	0.382s	2.568e 5	0.435s	0.0968

TABLE IV
QUANTITATIVE COMPARISON OF THE THREE OBSERVERS

Contents	$\hat{J}_m$		$\hat{T}_f$	
	CT(s)	RMSE	CT(s)	RMSE
Fig. 8 on DESMO	0.246s	0.787e 5	0.285s	0.0893
Fig. 9(a) on PESMO	1.102s	3.152e 5	0.688s	0.1508
Fig. 9(b) on VSESMO	1.507s	4.703e 5	1.081s	1.352
Fig. 9(c) on TESMO	0.741s	2.889e 5	0.454s	0.2296

TABLE V
EXECUTION TIME COMPARISON OF DIFFERENT OBSERVERS

Methods	DESMO	PESMO	VSESMO	TESMO
AET(μs)	2.64μs	3.59μs	2.28μs	2.37μs

the derivative of the estimated value equals zero. Varying degrees of estimation delay observed in the simulations further confirm this. Specifically, at 5 s, the system inertia is changed to $2.74 \times 10^{-4} + 0.2 \times 10^{-4} \cos(2\pi \cdot 0.5 \cdot t)$ to simulate the slow-varying inertia in practical applications. It is evident that the proposed observer achieves accurate identification results, while the other three observers exhibit significant chattering effects, particularly TESMO. This is primarily due to the stringent update mechanism for inertia estimation imposed by the robust activator, leading to certain instabilities. In addition, Table III presents a quantitative comparison of the estimation results for these observers in terms of convergence time (CT) and root mean square error (RMSE), which further validates the abovementioned analysis.

Next, to further validate the dynamic decoupling effect of the proposed DESMO, we simulated the results with different parameters α_3 based on the initial parameter configuration. As stated in Fig. 5(a), the smaller the value of α_3, the smoother the estimation results, but with a decrease in estimation accuracy. Nevertheless, in all cases, the observer eventually converges to the actual value, which indicates that the proposed DESMO exhibits superior decoupling performance in both transient and steady-state processes. In contrast, as shown in Fig. 5(b), for the TESMO, the estimation results with different activation threshold values Δ_ω exhibit significant steady-state differences. For example, when $\Delta_\omega = 0.2$, the unstable estimation result appear in the inertia estimation results. This is due to the fact that the activator, which has not been introduced into the stability proof of the observer, may cause instability of estimation results. It is noted that for too large α_3, i.e., when $\alpha_3 = 4$, the estimation results $\hat{J}_m$ and $\hat{T}_f$ appear to be slightly coupled. As a

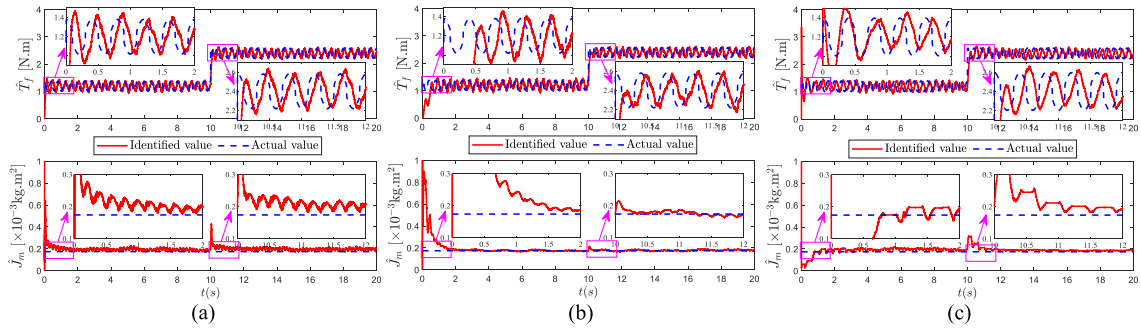

Fig. 9. Experimental results of the compared methods. (a) PESMO in [22]. (b) VSESMO in [25]. (c) TESMO in [23].

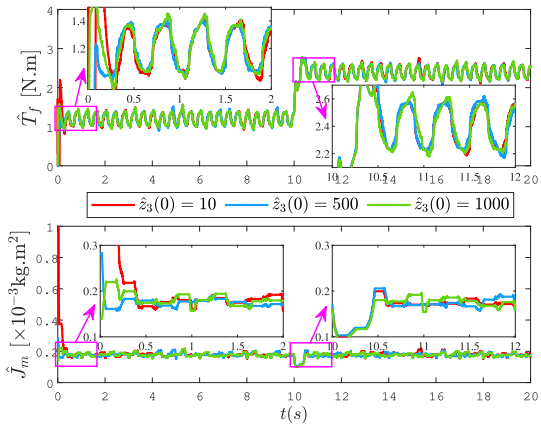

Fig. 10. Experimental results with different initial values.

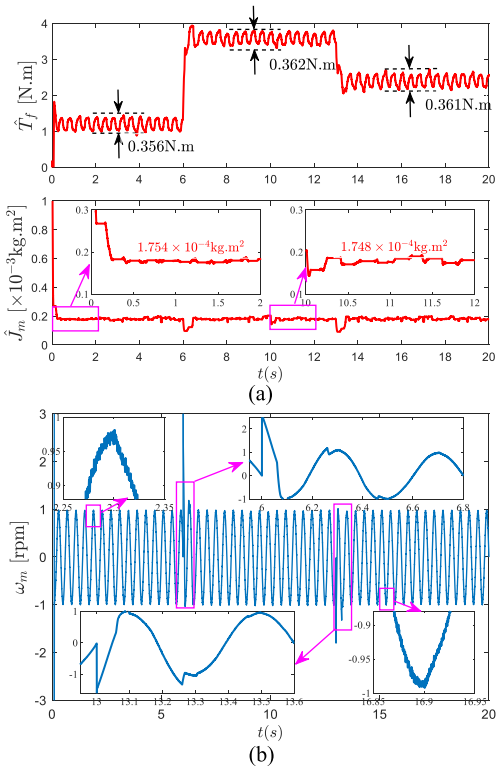

Fig. 11. (a) Parameter estimation resutls. (b) Speed response error after PI parameter tuning with disturbance compensation.

consequence, as a key configuration parameter in the DOCs, in addition to being crucial for decoupling the states of the estimation process, a reasonable tuning of α_3 is essential for the improvement of the estimation performance.

B. Modeling of Friction Torque

In order to test the estimation accuracy of the observer in the subsequent experimental part, it is necessary to get a more accurate value of the load disturbance under the overall working condition. From (1), the load disturbance T_f is mainly composed of load torque and friction torque, where the former is known and the latter is unknown. Therefore, under no-load conditions, two sets of unidirectional speed responses are required to fit the data curve relating to the electromagnetic torque T_e [22]. The viscous friction coefficient B and Coulomb friction coefficient C estimated from Fig. 6 are $4 \times 10^{-4}\,\mathrm{N{\cdot}m{\cdot}s{\cdot}rad^{-1}}$ and $0.06\,\mathrm{N{\cdot}m}$, respectively. Hence, the actual value of load disturbance obtained in the experimental part can be approximated as $T_f = 4 \times 10^{-4}\omega_m + 0.06\mathrm{sgn}(\omega_m) + T_L$.

C. Experimental Result

1) Experimental Bench Introduction and Parameter Configuration: We next further test the performance of the proposed method by the experimental platform displayed in Fig. 7 with the parameters shown in Table I, and the experimental parameter configurations of these observers are given by Table II. The hardware platform consists of the following five key components.

1) *Host PC*: Serves as the interface for system monitoring and control. It is responsible for parameter tuning, signal visualization, and real-time debugging, ensuring the smooth operation and adaptability of the system during experiments.
2) *Controller*: Built on the TMS320F28335 chip, the controller handles computational tasks and communicates with the servo driver through a high-speed CAN bus. A 1024 PPR incremental encoder is integrated to provide precise real-time feedback on rotor velocity and position.
3) *Servo driver*: Featuring the T1 TMS320F28069 chip, the servo driver ensures accurate velocity control by executing closed-loop control algorithms. This driver forms the

backbone of the system's dynamic response to control inputs.

4) *Magnetic powder brake*: A PB-type magnetic powder brake is installed on the load side to simulate dynamic load conditions. By adjusting the excitation current, it provides precise control of the load torque T_L, enabling the evaluation of system performance under varying disturbance levels.
5) *Torque sensor*: The WTQ1050 series sensor provides high-precision measurements of load disturbances, offering valuable data for control system validation and analysis.

2) Analysis and Comparison of Experimental Results: Due to the limitation that the experimental equipment is not capable of time-varying inertia conditions, we have only targeted the load torque T_L to abruptly change from $1.2\,\mathrm{N\cdot m}$ to $2.4\,\mathrm{N\cdot m}$ at $t = 10\,\mathrm{s}$. Figs. 8 and 9 present the experimental results, demonstrating the substantial challenges introduced by noise and nonlinearities, which significantly complicate the estimation process for these observers compared to the simulation results. Nevertheless, the proposed DESMO demonstrates consistently stable and accurate estimation results, whereas the other three observers show suboptimal performance, such as phase delays in time-varying load disturbance estimation, as well as oscillation phenomena in inertia estimation results. As the quantitative comparison exhibited in Table IV, the proposed DESMO is capable of achieving high-performance parameter identification in terms of CT and root mean square error (RMSE). It can be obtained that both the DESMO and TESMO achieve convergence to stable values within 0.8 s, while the other two observers, due to the coupling characteristics between states, require over 1 s to reach convergence. In addition, compared to the RMSE values of PESMO, VSESMO, and TESMO, the proposed DESMO achieves superior performance by reducing the RMSE of inertia estimation and load disturbance estimation to below 1×10^{-5} and 0.1, respectively.

In addition, Table V shows the algorithm execution time (AET) for each observer, from which it can be seen that the PESMO in [22] is the most time-consuming observer due to the computation involving two observers. In comparison, the execution time of our proposed DESMO is similar to that of the other two observers, at 2.64 μs.

3) Performance Evaluation With Different Initial Values: Testing the DESMO with different initial values of inertia can provide an effective way to validate its robustness and convergence performance. In our experiments, our observer is initialized with various incorrect initial values of inertia to simulate conditions where the actual inertia is not precisely known. Since the initial of $\hat{z}_3(0)$ can directly affect the initial of $\hat{z}_2(0)$, we only test for the case with different $\hat{z}_3(0)$ values. From the experimental results shown in Fig. 10, we can see that our DESMO has good adaptive ability and dynamic performance in the face of different initial values.

4) Control Effect Evaluation: To assess the impact of the parameters estimated by our DESMO on control performance, feedforward compensation is implemented using the real-time $\hat{T}_f$, while the estimated moment of inertia $\hat{J}_m$ is employed for PI parameter tuning. Specifically, the proportional gain k_p and integral gain k_i of the speed-loop controller are designed as $k_p = \hat{J}_m 60\pi$ and $k_i = \hat{J}_m (60\pi)^2/5$ [25]. In the initial stage, the load torque is added to $1.2\,\mathrm{N\cdot m}$ by the magnetic particle brake and then changed to $3.6\,\mathrm{N\cdot m}$ and $2.4\,\mathrm{N\cdot m}$ at 6 s and 13 s, respectively. Fig. 11 presents the experimental results of estimation parameter and the speed response error after PI parameter tuning with disturbance compensation. It can be observed that the parameter tuning based PI controller ensures significant control performance, maintaining the speed error within 1 r/min. Furthermore, the real-time compensation for load disturbance T_f effectively mitigates the impact of load torque and nonlinear disturbances on the system.

VI. Conclusion

This article proposes a DESMO for simultaneously estimating moment of inertia and load disturbance in a PMSM drive system. For the DOCs designed by the Lyapunov idea, the stability of the resulting two-update equations has been verified by detailed theoretical analysis. Simulation and experimental results validate the observer's effectiveness in real-time estimation, even under dynamic estimation state conditions. Integrated into a PI control framework, the observer enhances system performance with simplicity and robustness. Compared with the state of the art SMOs, in addition, our DEMO is capable of realizing high-quality estimation performances in terms of convergence speed, identification accuracy, and robustness. In future work, we will explore the use of the super-twisting algorithm in the DESMO to further enhance its performance. In addition, we plan to extend the observer's application to advanced controllers, such as model predictive control, and evaluate its performance in more complex systems.

Appendix A
Proof of Theorem 2

Proof: The time derivative of $V_{z1}(t)$ is performed to yield

$$\begin{aligned}\dot{V}_{z1}(t) &= \dot{\varepsilon}^{\mathrm{T}}(t)P_{z1}(t)\varepsilon(t) + \varepsilon^{\mathrm{T}}(t)P_{z1}(t)\dot{\varepsilon}(t) \\ &\quad + \varepsilon^{\mathrm{T}}(t)\dot{P}_{z1}(t)\varepsilon(t) \\ &= \varepsilon^{\mathrm{T}}(t)[A^{\mathrm{T}}{}_{z1}(t)P_{z1}(t) + P_{z1}(t)A^{\mathrm{T}}{}_{z1}(t) \\ &\quad + \dot{P}_{z1}(t)] \cdot \varepsilon(t) + B^{\mathrm{T}}{}_{z1}(t)P_{z1}(t)\varepsilon(t) \\ &\quad + \varepsilon^{\mathrm{T}}(t)P_{z1}(t)B_{z1}(t) \\ &= \varepsilon^{\mathrm{T}}(t)[\dot{P}_{z1}(t) - I_2]\varepsilon(t) + B^{\mathrm{T}}{}_{z1}(t)P_{z1}(t)\varepsilon(t) \\ &\quad + \varepsilon^{T}(t)P_{z1}(t)B_{z1}(t). \end{aligned} \tag{42}$$

In line with (31) and (36), one can get

$$\begin{aligned}\dot{V}_{z1}(t) &\le \varepsilon^{\mathrm{T}}(t)[\dot{P}_{z1}(t) - I_2]\varepsilon(t) + \varepsilon^{\mathrm{T}}(t)\phi(t)\varepsilon(t) \\ &\quad + B^{\mathrm{T}}{}_{z1}(t)P_{z1}(t)\varepsilon(t) + \varepsilon^{\mathrm{T}}(t)P_{z1}(t)B_{z1}(t) \\ &\quad le(\kappa - I_2)\left\|\varepsilon(t)\right\|^2 + 2N_8\left\|\varepsilon(t)\right\|. \end{aligned} \tag{43}$$

Due to $\lambda_{\min}\{P_{z1}\}\|\varepsilon(t)\|^2 \leq V_{z1}(t) \leq \lambda_{\max}\{P_{z1}\}\|\varepsilon(t)\|^2$, rewriting (43) yields

$$\dot{V}_{z1}(t) \leq (\kappa - I_2)\lambda_{\max}^{-1}\{P_{z1}\}V_{z1}(t) + 2N_8\lambda_{\min}^{-\frac{1}{2}}\{P_{z1}\}V_{z1}^{\frac{1}{2}}(t). \tag{44}$$

Next, (44) can be further processed as

$$\dot{V}_{z1}^{\frac{1}{2}}(t) \leq \frac{(\kappa - I_2)}{2}\lambda_{\max}^{-1}\{P_{z1}\}V_{z1}^{\frac{1}{2}}(t) + N_8\lambda_{\min}^{-\frac{1}{2}}\{P_{z1}\}. \tag{45}$$

Hence, (45) is solved as

$$V_{z1}^{\frac{1}{2}}(t) \leq [V_{z1}^{\frac{1}{2}}(0) + \frac{2N_8}{(\kappa - I_2)}\lambda_{\min}^{-\frac{1}{2}}\{P_{z1}\}\lambda_{\max}\{P_{z1}\}] \cdot e^{\frac{(\kappa-I_2)}{2}\lambda_{\max}^{-1}\{P_{z1}\}t} - \frac{2N_8}{(\kappa - I_2)}\lambda_{\min}^{-\frac{1}{2}}\{P_{z1}\}\lambda_{\max}\{P_{z1}\}. \tag{46}$$

Finally, rewrite (46) to get

$$\|\varepsilon(t)\| \leq [V_{z1}^{\frac{1}{2}}(0)\lambda_{\min}^{-\frac{1}{2}}\{P_{z1}\} + \frac{2N_8\lambda_{\max}\{P_{z1}\}}{(\kappa - I_2)\lambda_{\min}\{P_{z1}\}}] \cdot e^{\frac{(\kappa-I_2)}{2}\lambda_{\max}^{-1}\{P_{z1}\}t} - \frac{2N_8\lambda_{\max}\{P_{z1}\}}{(\kappa - I_2)\lambda_{\min}^{\frac{1}{2}}\{P_{z1}\}}. \tag{47}$$

As a consequence, one conclusion can be drawn that the errors, $\tilde{z}_2(t)$ and $\tilde{z}_2(t)$, converge exponentially with consistent eventually bounded, i.e., satisfying

$$\tilde{z}_{2,3}(t) \leq V_{z1}^{\frac{1}{2}}(0)\lambda_{\min}^{-\frac{1}{2}}\{P_{z1}\} - \frac{2N_8\lambda_{\max}\{P_{z1}\}}{(\kappa - I_2)\lambda_{\min}^{\frac{1}{2}}\{P_{z1}\}} \text{ for } t \geq 0. \tag{48}$$

Therefore, the proof of Theorem 2 is completed.

REFERENCES

[1] L. Qin, Y. Tian, Y. Yang, J. L. Soon, and W. Hassan, "Transformer-less two-phase interleaved boost converter with wide input voltage range and low electric stress for fuel cell vehicles," *IEEE Trans. Power Electron.*, vol. 40, no. 4, pp. 5480–5495, Apr. 2025, doi: 10.1109/TPEL.2024.3509524.

[2] S. Zheng, Y. Zha, C. K. Ahn, S. Lu, and B. Song, "Constrained finite-time output regulation for robot manipulators with input delay," *IEEE/ASME Trans. Mechatron.*, to be published, doi: 10.1109/TMECH.2025.3527751.

[3] K. Liu and Z. Zhu, "Fast determination of moment of inertia of permanent magnet synchronous machine drives for design of speed loop regulator," *IEEE Trans. Control Syst. Technol.*, vol. 25, no. 5, pp. 1816–1824, Sep. 2017.

[4] C. Yang, B. Song, Y. Xie, S. Lu, and X. Tang, "Speed-controller-independent mechanical parameter identification in SPMSM drive achieved via signal injection," *IEEE Trans. Ind. Electron.*, vol. 70, no. 2, pp. 1282–1297, Feb. 2023.

[5] J. Yang, W.-H. Chen, S. Li, L. Guo, and Y. Yan, "Disturbance/uncertainty estimation and attenuation techniques in PMSM drives—A survey," *IEEE Trans. Ind. Electron.*, vol. 64, no. 4, pp. 3273–3285, Apr. 2017.

[6] C. Wang, J. Liu, L. Xin, G. Li, and J. Pan, "Design of full-order state observer for two-mass joint servo system based on the fixed gain filter," *IEEE Trans. Power Electron.*, vol. 37, no. 9, pp. 10466–10475, Sep. 2022.

[7] Z. Yin, R. Tang, C. Du, and Y. Wang, "Moment of inertia identification based on unscented Kalman filter for permanent magnet synchronous motors," in *Proc. 14th IEEE Conf. Ind. Electron. Appl.*, 2019, pp. 1141–1145.

[8] L. Niu, D. Xu, M. Yang, X. Gui, and Z. Liu, "On-line inertia identification algorithm for PI parameters optimization in speed loop," *IEEE Trans. Power Electron.*, vol. 30, no. 2, pp. 849–859, Feb. 2015.

[9] M. Xie, J. She, Z.-T. Liu, and D.-Y. Li, "Online estimation of moment of inertia incorporating disturbance estimation," *IEEE Trans. Ind. Electron.*, vol. 71, no. 7, pp. 7610–7620, Jul. 2024, doi: 10.1109/TIE.2023.3314912.

[10] X. Zhang and Z. Li, "Sliding-mode observer-based mechanical parameter estimation for permanent magnet synchronous motor," *IEEE Trans. Power Electron.*, vol. 31, no. 8, pp. 5732–5745, Aug. 2016.

[11] C. Lian, F. Xiao, S. Gao, and J. Liu, "Load torque and moment of inertia identification for permanent magnet synchronous motor drives based on sliding mode observer," *IEEE Trans. Power Electron.*, vol. 34, no. 6, pp. 5675–5683, Jun. 2019.

[12] Q. Hou and S. Ding, "Finite-time extended state observer-based super-twisting sliding mode controller for PMSM drives with inertia identification," *IEEE Trans. Transp. Electrific.*, vol. 8, no. 2, pp. 1918–1929, Jun. 2022.

[13] C. Cao, S. Lu, S. Zheng, and B. Song, "Antisaturation extended state observer for speed predictive control of servo system," *IEEE Trans. Power Electron.*, vol. 39, no. 8, pp. 9318–9328, Aug. 2024.

[14] S. Li and H. Gu, "Fuzzy adaptive internal model control schemes for PMSM speed-regulation system," *IEEE Trans. Ind. Inform.*, vol. 8, no. 4, pp. 767–779, Nov. 2012.

[15] S. Li and Z. Liu, "Adaptive speed control for permanent-magnet synchronous motor system with variations of load inertia," *IEEE Trans. Ind. Electron.*, vol. 56, no. 8, pp. 3050–3059, Aug. 2009.

[16] J. Chen and J. Huang, "Alternative solution regarding problems of adaptive observer compensating parameters uncertainties for sensorless induction motor drives," *IEEE Trans. Ind. Electron.*, vol. 67, no. 7, pp. 5879–5888, Jul. 2020.

[17] Y. Chen, M. Yang, J. Long, W. Qu, D. Xu, and F. Blaabjerg, "A moderate online servo controller parameter self-tuning method via variable-period inertia identification," *IEEE Trans. Power Electron.*, vol. 34, no. 12, pp. 12165–12180, Dec. 2019.

[18] C. Yang, B. Song, Y. Xie, S. Lu, and X. Tang, "Stable simultaneous inertia and disturbance torque identification for SPMSM drive systems subject to mismatched rotor flux linkage," *IEEE J. Emerg. Sel. Topics Power Electron.*, vol. 10, no. 2, pp. 2445–2462, Apr. 2022.

[19] C. Yang, B. Song, Y. Xie, S. Zheng, and X. Tang, "Adaptive identification of nonlinear friction and load torque for PMSM drives via a parallel-observer-based network with model compensation," *IEEE Trans. Power Electron.*, vol. 38, no. 5, pp. 5875–5897, May 2023.

[20] D. Xiang, J. Yang, Y. Hao, and G. Xu, "Parallel-cascaded parameter identification scheme for PMSM-driven servo systems during self-commission," *IEEE Trans. Ind. Electron.*, vol. 72, no. 2, pp. 1914–1924, Feb. 2025, doi: 10.1109/TIE.2024.3417983.

[21] H. Chang, S. Lu, S. Zheng, B. Song, and J. Yang, "Integration of predictive control and interconnected structure for autotuning velocity controller," *IEEE/ASME Trans. Mechatron.*, vol. 28, no. 6, pp. 3250–3262, Dec. 2023.

[22] C. Yang, B. Song, Y. Xie, and X. Tang, "Online parallel estimation of mechanical parameters for PMSM drives via a network of interconnected extended sliding-mode observers," *IEEE Trans. Power Electron.*, vol. 36, no. 10, pp. 11818–11834, Oct. 2021.

[23] L. Wang, Z. Tang, P. Zhang, X. Liu, D. Wang, and X. Li, "Double extended sliding-mode observer-based synchronous estimation of total inertia and load torque for PMSM-driven spindle-tool systems," *IEEE Trans. Ind. Informat.*, vol. 19, no. 7, pp. 8496–8507, Jul. 2023.

[24] S. Tang, Y. Cao, T. Shi, Y. Yan, and C. Xia, "Online estimation of load torque and moment of inertia incorporating extended disturbance observer with trigger," *IEEE Trans. Power Electron.*, vol. 40, no. 4, pp. 5731–5742, Apr. 2025, doi: 10.1109/TPEL.2024.3509863.

[25] S. Tang, T. Shi, Y. Cao, Z. Lin, Z. Wang, and Y. Yan, "Simultaneous identification of load torque and moment of inertia of PMSM based on variable structure extended sliding mode observer," *IEEE Trans. Power Electron.*, vol. 39, no. 7, pp. 8585–8596, Jul. 2024.

[26] S. Kim, "Moment of inertia and friction torque coefficient identification in a servo drive system," *IEEE Trans. Ind. Electron.*, vol. 66, no. 1, pp. 60–70, Jan. 2019.

He Chang (Student Member, IEEE) received the M.E. degree in control engineering from the Wuhan University of Science and Technology, Wuhan, China, in 2023. He is currently working toward the Ph.D. degree in electronic information with the School of Automation, Southeast University, Nanjing, China.

His research interests include system identification, adaptive control, and their applications to ac motor system and sustainable energy system.

Zuo Wang (Member, IEEE) received the B.Eng. degree in automation from Hohai University, Nanjing, China, in 2013, and the Ph.D. degree in automatic control from Southeast University, Nanjing, China, in 2020.

Since 2020, he has been with the School of Automation, Southeast University, where he is currently a Postdoctoral Researcher. His research interests include advanced control theory and its application to power electronics, ac motor control systems, and spacecraft attitude systems.

Jun Yang (Fellow, IEEE) received the B.Sc. degree in automation from the Department of Automatic Control, Northeastern University, Shenyang, China, in 2006, and the Ph.D. degree in control theory and control engineering from the School of Automation, Southeast University, Nanjing, China, in 2011.

He joined the Department of Aeronautical and Automotive Engineering, Loughborough University, Loughborough, U.K., where he has been a Senior Lecturer since 2020. His research interests include disturbance observer, motion control, visual servoing, nonlinear control, and autonomous systems.

Dr. Yang is currently an Associate Editor or Technical Editor for IEEE TRANSACTIONS ON INDUSTRIAL ELECTRONICS, IEEE-ASME TRANSACTIONS ON MECHATRONICS, IEEE Open Journal of Industrial Electronics Society, etc. He was the recipient of the EPSRC New Investigator Award. He is also a Fellow of IET.

Shihua Li (Fellow, IEEE) received the B.S., M.S., and Ph.D. degrees in automatic control from Southeast University, Nanjing, China, in 1995, 1998, and 2001, respectively.

Since 2001, he has been with the School of Automation, Southeast University, where he is currently a Full Professor and the Director of Mechatronic Systems Control Laboratory. His main research interests lie in modeling, analysis and nonlinear control theory with applications to mechatronic systems, including robot, ac motor, engine control, power electronic systems, and others.

Shaowu Lu received the Ph.D. degree in mechanical engineering from the Huazhong University of Science and Technology, Wuhan, China, in 2013.

He is currently a Professor with the Wuhan University of Science and Technology, Wuhan, China. His current research interests include system identification and intelligent control.